To appear in the *Journal of Geophysical Research*, 2001.

Thermal Emission Spectrometer results: Mars atmospheric thermal structure and aerosol distribution

Michael D. Smith and John C. Pearl
NASA Goddard Space Flight Center, Greenbelt, Maryland

Barney J. Conrath
Center for Radiophysics and Space Research, Cornell University, Ithaca, New York

Philip R. Christensen
Department of Geology, Arizona State University, Tempe

Abstract

Infrared spectra returned by the Thermal Emission Spectrometer (TES) are well suited for retrieval of the thermal structure and the distribution of aerosols in the Martian atmosphere. Combined nadir- and limb-viewing spectra allow global monitoring of the atmosphere up to 0.01 mbar (65 km). We report here on the atmospheric thermal structure and the distribution of aerosols as observed thus far during the mapping phase of the Mars Global Surveyor mission. Zonal and temporal mean cross sections are used to examine the seasonal evolution of atmospheric temperatures and zonal winds during a period extending from northern hemisphere mid-summer through vernal equinox ($L_s = 104°$–$360°$). Temperature maps at selected pressure levels provide a characterization of planetary-scale waves. Retrieved atmospheric infrared dust opacity maps show the formation and evolution of regional dust storms during southern hemisphere summer. Response of the atmospheric thermal structure to the changing dust loading is observed. Maps of water-ice clouds as viewed in the thermal infrared are presented along with seasonal trends of infrared water-ice opacity. Uses of these observations for diagnostic studies of the dynamics of the atmosphere are discussed.

1. Introduction

The Thermal Emission Spectrometer (TES) onboard the Mars Global Surveyor (MGS) is a versatile instrument with scientific objectives in both geology and atmospheric science. Results pertaining to geology and polar science are described in a companion paper by *Christensen et al* [this issue]. In the present paper we describe results relating to atmospheric science obtained from the TES during its first Earth year in mapping orbit.

The principal atmospheric scientific objectives for the Thermal Emission Spectrometer are to determine (1) the composition, particle size, and spatial and temporal distribution of suspended dust, (2) the location, temperature, height, and water abundance of H_2O clouds, and (3) the thermal structure (temperature vs. height) of the atmosphere as a function of location and season [*Christensen et al.*, 1992]. Analysis of spectra returned from TES during the first Earth-year of mapping has yielded significant results relating to each of the above objectives.

Even before achieving mapping orbit, data from TES have produced a wealth of information about the atmosphere of Mars. Preliminary findings from the first portion of MGS aerobraking are described by *Christensen et al.* [1998]. An overview of observations of dust opacity during MGS aerobraking and science phasing (which covers all observations prior to those covered in this paper) is given by *Smith et al.* [2000a], and the opacity of dust and water-ice aerosol as a function of frequency has been derived by *Smith et al.* [2000b] and *Bandfield et al.* [2000]. A description of water-ice clouds observed by TES is given by *Pearl et al.* [2000]. The thermal structure of the atmosphere during MGS aerobraking and science phasing is described by *Conrath et al.* [2000] and *Clancy et al.* [2000]. Finally, an analysis of thermal tides and stationary waves based on TES data is given by *Banfield et al.* [2000]. An overview of results from the Mariner and Viking missions relating to the Mars atmosphere are given by *Zurek et al.* [1992] and *Kahn et al.* [1992]. Atmospheric results from the Mars Pathfinder are given by *Schofield et al.* [1997], *Magalhães et al.* [1999], and *Smith and Lemmon* [1999].

In the next section we give a brief description of the TES instrument and the data taken during the mapping orbit. More detailed information is given by *Christensen et al.* [1992; this issue]. In section 3, we give a general overview of atmospheric thermal structure and aerosol distribution observed by TES during MGS mapping showing the interrelations between the quantities. In Section 4, we present a more detailed look at the dust storms observed by TES during the period, as well as the low-latitude belt of water-ice clouds observed during the aphelion season. In Section 5, we show how the atmospheric thermal structure and the inferred wind fields vary with season and we also show some examples of the waves observed by TES in the atmosphere. We summarize our findings in Section 6.

2. Data Set

2.1. TES Instrument

The Thermal Emission Spectrometer (TES) is an infrared interferometer/spectrometer with additional broadband visible and thermal channels [*Christensen et al.*, 1992]. Six detectors in a three-by-two array simultaneously take spectra covering the spectral range from 200 to 1600 cm^{-1} (6–50 μm), with a selectable sampling of either 5 or 10 cm^{-1} (a large majority of the data collected so far has 10-cm^{-1} sampling). A pointing mirror allows TES to view from nadir to above both the forward and aft limbs, where the atmosphere is observed without direct contribution from the surface. Each pixel subtends an 8.3-mrad field of view, giving a spatial resolution of 3x9 km after accounting for smear caused by spacecraft motion.

2.2. TES Observations During Mapping

The Mars Global Surveyor mapping orbit gives one narrow (three-pixel-wide) strip of observations running roughly north-south. One day of data gives two sets of twelve such strips spaced roughly 30° apart in longitude, with one set taken near 2:00 PM and the other near 2:00 AM local time. The primary mode of TES data acquisition is with the field-of-view pointed toward nadir. However, every 10° of latitude around the orbit, a sequence of limb-geometry observations is taken with the field-of-view pointed to observe the atmosphere above the limb. Because the nadir-geometry observations are far more numerous, they are used for mapping the spatial distribution of aerosol opacities. Retrieval of the atmospheric thermal structure uses a combination of observations with nadir-geometry spectra giving information about the lowest 30 km above the surface, and limb-geometry spectra giving information from roughly 30-65 km.

The results presented below were derived using data starting with the beginning of the mapping por-

tion of the MGS mission at L_s = 104° (March 1, 1999) to the beginning of the new Martian year at L_s = 0° (June 1, 2000). TES operated nearly continually during this entire period with only minor exceptions. This has resulted in several tens of millions of spectra, giving an unprecedented combination of spatial and temporal coverage.

3. Overview of Atmospheric Conditions

To provide an overview of the atmospheric state over the entire MGS mapping mission to this point, we have produced maps of dust opacity, water-ice opacity, and the atmospheric temperature at 0.5 mbar (about 25 km above the surface) by binning in latitude and season (L_s). The bins in latitude are 5° wide, and the bins in L_s cover one mapping day or 12 orbits (a little more than 0.5° of L_s). Only dayside (local time about 2:00 PM) data are used for all three quantities. The dust opacities have been scaled to a 6.1 mbar equivalent pressure surface to remove the effect of topography which often dominates the spatial distribution of dust. Water-ice opacities are not scaled since water-ice opacity is not closely proportional to the total atmospheric column mass (surface pressure). Each data bin (in latitude and L_s) typically contains the average of several hundred individual retrievals of temperatures and aerosol opacity.

3.1. Retrieval Methods

A detailed description of the retrieval algorithms for atmospheric temperatures and aerosol opacities is given by *Smith et al.* [2000a] (dust opacity), *Pearl et al.* [2000] (water-ice opacity), and *Conrath et al.* [2000] (atmospheric temperatures). Here we describe the retrievals in outline. The retrievals of atmospheric temperature and aerosol opacity are performed sequentially. Atmospheric temperatures are retrieved using a constrained linear inversion of radiance in the 15-μm CO_2 band. In this retrieval we have accounted for aerosol opacity to first order by using an effective surface temperature calculated by taking the brightness temperatures in narrow spectral intervals on either side of the CO_2 band and averaging them. The spectral intervals are 508–529 and 814–825 cm^{-1}. Temperatures from the surface to about 0.1 mbar (35 km) are obtained from nadir-geometry spectra with a typical vertical resolution of about one scale height (10 km). Temperature profiles can be extracted from 1.0 to 0.01 mbar (65 km) where limb-geometry spectra are available (typically every 10° in latitude). Complete temperature profiles to 0.01 mbar are obtained by splicing the two temperature profiles through averaging in the 0.1 to 1.0 mbar range. Individual temperature profiles have a typical uncertainty of about 2 K except in the lowest scale height above the ground where the uncertainty is somewhat larger.

Aerosol opacities are retrieved after the temperature retrieval is performed. To do so we first compute the equivalent column-integrated opacity of a pure absorber as a function of wavenumber. Then, we estimate the contribution of dust and water ice to the total opacity by performing a least-squares fit of predetermined spectral shapes (opacity as a function of wavenumber) for dust, water ice, and the effect of a nonunit emissivity surface to the observed opacity spectrum. The predetermined spectral shapes for dust and water ice are determined from TES data and are described by *Smith et al.* [2000b] and *Bandfield et al.* [2000]. The retrieval of aerosol opacities is restricted to those spectra with a surface temperature greater than 220 K. This constraint ensures that there is sufficient thermal contrast between the surface and the atmosphere for an accurate retrieval.

The retrieval of aerosol opacity uses two major simplifying assumptions. We assume that 1) the aerosol is well-mixed with the CO_2 gas, and that 2) the aerosols are nonscattering. The first assumption has been found to be good for dust in Viking [*Pollack et al.*, 1977], Pathfinder [*Smith et al.*, 1997], and TES data [*Smith et al.*, 2000a]. However, water-ice often present in stratified clouds [*Pearl et al.*, 2000]. Numerical experiments show that for typical daytime conditions opacities can be overestimated by 20–50%. This uncertainty does not affect the identification of water-ice clouds or our statistics on their occurrence with season or location. But, until we have a better understanding from limb-geometry observations about the heights and temperatures at which water-ice clouds form, we do not feel we should attempt to correct for this bias.

The second assumption, that the aerosols are nonscattering, has been shown to be good to 10–20% when aerosol opacities are not too large [*Smith et al.*, 2000a]. During the dustiest times (dust storms), when opacity reaches unity or higher, scattering becomes more important, and the opacity estimates presented here become more of an indicator of relative dust opacity than an absolute measure of the amount of dust in the atmosphere. Overall, the estimated uncertainty for any one opacity retrieval is ±0.05, for

opacities less than 0.5.

3.2. Discussion

In Plate 1, the top panel shows temperatures at 0.5 mbar (25 km), the middle panel shows dust opacity at 1075 cm^{-1}, and the bottom panel shows water-ice opacity at 825 cm^{-1}. Apparent in the temperature panel is the seasonal warming of the atmosphere as Mars moves from near aphelion at the beginning of mapping to perihelion during southern hemisphere summer. Also apparent are several episodes of heating with onsets at L_s =140°, 180°, 225°, and 260° associated with dust storms. The largest dust storm at L_s =225° caused the northern and southern mid-latitude atmosphere to warm by 15 K. The temperature increase in the southern hemisphere is caused by direct solar heating from increased levels of suspended dust. The temperature increase in the northern hemisphere is primarily a dynamical effect caused by an increase in the strength of the cross-equatorial Hadley cell. Both heatings occur almost simultaneously and have comparable amplitudes. Very similar behavior was also observed in the previous Mars year with the large regional Noachis dust storm of November 1997 [*Smith et al.*, 2000a]. The heating event at L_s =260° at high southerly latitudes has similar amplitude and is again caused by a large increase in dust opacity. However, this storm does not show a corresponding increase in northern hemisphere temperatures or dust, apparently because the dust storm was too far south to effectively intensify the Hadley circulation.

The dust activity shown in the center panel of Plate 1 indicates a dust storm season with only moderate activity. Averaged dust opacity was comparable to the previous Mars year observed by TES (1997–1998) [*Smith et al.*, 2000a], but substantially less than that observed during the first Viking year [*Martin and Richardson*, 1993; *Martin*, 1986] or by Mariner 9 [*Fenton et al.*, 1997, *Hanel et al.*, 1972]. Five regional dust storms of moderate to large size can be seen in this Plate. The first began around L_s =160° at around 50° S latitude and persisted at a moderate level (average scaled opacity of 0.3–0.4) until L_s=200°. The dust storm activity between L_s =225° and 245° is the result of two principal storm centers, as will be discussed in more detail in the next section. These two storms were active at the same time and were the two largest dust storms observed during this dust storm season. Each had opacities reaching unity in their respective cores, but neither reached global scale, and the combined force of both storms did not produce a globally-averaged opacity as large as that produced by the Noachis dust storm of 1997. A fourth regional dust storm began poleward of 70° S latitude just before L_s =260°. Although this dust storm had locally high opacities (reaching unity), it did not spread northward. The last regional dust storm observed was active during the period L_s=320°–350°. Although relatively large in extent, the storm reached only moderate opacity levels (zonally averaged value of about 0.4) and did not spread in latitude or affect atmospheric temperatures significantly.

The bottom panel of Plate 1 shows the occurrence and location of water-ice clouds. The most striking feature is the low-latitude belt of clouds extending from 10° S to 30° N latitude from the beginning of mapping (L_s =104°) to L_s =145°. This aphelion season cloud belt is also discussed by *Pearl et al.* [2000], and similar water-ice cloud belts have been observed in previous years (for example, [*Wolff et al.*, 1999; *Clancy et al.*, 1996; *James et al.*, 1994]). The cloud opacity decreased abruptly at L_s =145°, although a preference for water-ice clouds at low latitudes persists throughout the year because of the location of the Tharsis and Elysium topographic features. Beginning at L_s =160°, the formation of the polar hood is seen at mid-northerly latitudes at the edge of the data shown in Plate 1. A weaker polar hood smaller in latitude extent is also indicated in the south during southern winter. Except in the northern polar hood, the temperature increase at L_s =225° associated with the two large regional dust storms moved the saturation level for water-ice clouds much higher in the atmosphere drastically reducing the column-integrated opacity of water-ice clouds in the atmosphere until L_s =280°.

4. Dust Storms and Water-Ice Clouds

Continuous global monitoring by TES has shown that dust and water-ice aerosols are nearly everywhere. Plate 1 shows that the amount of each varies with season in a systematic way, with higher average dust opacity (and more frequent regional dust storms) in the southern hemisphere summer, and higher average water-ice cloud opacity in a low-latitude belt during northern winter. Although the above general trend repeats from year to year, there is also significant interannual variability (for example, compare with [*Smith et al.*, 2000a; *Clancy et al.*, 2000; *Tamppari et al.*, 2000; *Wolff et al.*, 1999; *Fenton et al.*,

1997; *Clancy et al.*, 1996; *Martin and Richardson*, 1993; *Martin*, 1986]), and each dust storm is unique and evolves in its own way. Below we detail the behavior of the five largest regional dust storms observed by TES and the location in latitude and longitude of ice-cloud occurrence during opposite seasons.

4.1. Dust Activity Between L_s =225° and 245°

The two largest dust storms observed by TES occurred between L_s =225° and 245°. The set of maps in Plate 2 shows the initiation, evolution, and decay of these large regional dust storms. Each panel is a map of 1075 cm^{-1} (9-μm) dust opacity made from one mapping day of data (12 orbits). The effect of topography has been removed by scaling opacities to an equivalent 6.1 mbar pressure surface. The color scale is the same for each map. Blue and purple indicate low dust opacity (clear atmosphere), green indicates moderate dust opacity, and yellow and red indicate the high dust opacities associated with dust storms. The visible opacity of dust is about twice the 9-μm opacity shown here [*Clancy et al.*, 1995], so anywhere that is yellow or red on these maps there are dust clouds that are thick enough to obscure the surface in visible light.

The map for L_s =216.2° shows the clear conditions that existed prior to the beginning of the dust storms. At L_s =223.5°, TES observed the initiation of a regional dust storm near the equator and 0°–60° W longitude. By L_s =225.9° the dust storm had significantly intensified and grown. At this time the storm measured approximately 3000 km across. At L_s =227.8° the dust storm had stopped growing and a second regional dust storm had started centered at 180° W longitude. A smaller, local dust storm was also present centered at 60° S, 140° W near the edge of the retreating south polar cap. Four sols later, at L_s =230.2°, the first dust storm had significantly decreased in intensity and the second dust storm had migrated southward and intensified. By L_s =232.1° there was little left of the first dust storm; the second dust storm had expanded but had decreased somewhat in intensity. At L_s =235.1° the second regional dust storm had migrated further south and had reestablished itself near 60° S, 210° W. The dust storm intensified somewhat over the next few sols (L_s =237.0°) while dust opacities north of 40° S became very uniform at a moderate level (0.35). Over the next week or two (L_s =243.2°) the second dust storm finally dissipated, and throughout the next two weeks (L_s =250.0° and 256.3°) the entire atmosphere gradually cleared.

The initiation of these storms at L_s =223° was at very nearly the same season as the Noachis Dust Storm of November 1997 which began at L_s =225° [*Smith et al.*, 2000a]. The location of initiation of this year's dust storm (Margaritifer Terra, 0° N, 30° W) was somewhat to the northwest of the initiation site of the Noachis Dust Storm (Noachis Terra), but both started at low-southerly latitudes. Both dust storms expanded southward. This year, a second dust storm center appeared nearly 180° away from the original. This second storm became the principal source of dust activity and migrated to high southerly latitudes at 180°–240° W longitude. The Noachis Dust Storm expanded to nearly all longitudes once reaching 60° S latitude, but established a secondary core at the same longitudes. Another regional dust storm that occurred after the Noachis Dust Storm at L_s = 309° (April 1998) began at low-southerly latitudes and 20°–120° W longitude, spread to the south and east, and established a core of activity at 65°–80° S latitude, 180°–270° W longitude [*Smith et al.*, 2000a]. In all three cases the dust storms started at low latitudes, spread south and often preferentially to the east. All ended up with cores of activity at high southerly latitudes in the 180°–270° W longitude quadrant. The southward spread of these dust storms is qualitatively similar to the regional dust storm modeled by *Murphy et al.* [1995], but their modeling does not show a longitude preference at high-southerly latitudes.

4.2. Other Dust Storms

In addition to the two large regional dust storms described above, TES observed at least three other dust storms that were regional in scale. Plate 3 shows maps of these three dust storms. The first period of dust storm activity was between about L_s =170° and 190° and is shown in the top panel. The principal center of activity was in Hellas basin with smaller but significant dust storms in Argyre basin and along the edge of the retreating polar cap. The maps shown in Plate 3 have had the effect of topography removed by scaling to an equivalent 6.1 mbar surface but Hellas and Argyre still clearly show. At this time they were both very dusty compared to surrounding areas. By L_s =200° the increased dust activity in Hellas and Argyre had ended and dust activity along the south polar cap edge diminished. TES observed a similar sequence of events in the previous Martian

year (1997) as Hellas and Argyre filled with dust between L_s =184° and 194° and then cleared before the main part of the dust storm season began [*Smith et al.*, 2000a].

After the large dust storms of L_s =225°–245° had begun to clear, a new round of significant dust activity began at the edge of the south polar cap at about L_s =260° (middle panel of Plate 3). The entire edge of the polar cap was active with dust storms but with a preference for the hemisphere from 90°–270° W longitude. This ring of dust storms was very active with dust opacities exceeding 0.5 in a number of places. Encircling the ring of dust storms to the north (50°–60° S latitude) was a band of relatively low dust amount (opacities of 0.2). Dust from the large equatorial storms of L_s =225°–245° had redistributed itself over low- and mid-northern and southern latitudes to form a nearly uniform covering of dust with an opacity of about 0.3. This configuration was maintained until about L_s =280° when new activity along the south polar cap edge diminished and the atmosphere began to clear significantly at all latitudes. At the same time that the south polar ring of dust storms was active, a completely independent local dust storm was active in the northern hemisphere located between Olympus Mons and Alba Patera. The occurrence of local dust storms in this region, and in Amazonis Planitia to the west of Olympus Mons, was not an unusual event; several such storms were observed by TES during mapping, including another fairly large one in Amazonis between L_s =140° and 145°.

A final period of moderate dust activity began at L_s =321° and lasted for over a month (bottom panel of Plate 3). Beginning at around L_s =310° there was a mild increase in activity near the equator, especially between 0° and 80° W longitude. At L_s =321° the dust activity dramatically increased between 20° and 80° W longitude giving opacities approaching unity. This was the same location as the start of the large L_s =225° dust storm. But, although the L_s =321° dust storm had an intense core in the beginning it did not grow to nearly the size or extent of the L_s =225° dust storm. Through the month following the beginning of the L_s =321° dust storm there were several intensifications in dust activity at low latitudes. One dust storm was at L_s =329° centered near 10° N latitude, 240° W longitude, one was at L_s =335° centered near 30° N latitude, 50° W longitude (just to the north of the original dust storm center), and one was at L_s =335° centered near 10° N latitude, 180° W longitude. These dust storms subsided by L_s =345°, leaving a belt of dust at low latitudes with an opacity of about 0.25 to 0.3 (compared to 0.10 to 0.15 at mid- to upper-latitudes in the north and south).

4.3. Water-Ice Clouds

The occurrence of water-ice clouds on Mars in TES data is very common. At certain locations and times during the year the opacity of water-ice clouds is comparable or even exceeds that of dust (see Plate 1). Plate 4 contains maps showing the daytime (2:00 PM local time) spatial distribution of water-ice clouds during opposite seasons. The top panel shows the northern summer (near aphelion) season L_s =104°–140°. A belt of clouds between 10° S and 30° N latitude dominates the map, consistent with the latitude range where upward motions from a Hadley circulation would be expected for this season [*Clancy et al.*, 1996]. There is considerable longitudinal structure in the water-ice cloud belt shown in the map, and that structure was very repeatable from sol to sol during the entire period shown. There were consistently high water-ice cloud opacities over topographic highs of Tharsis, Olympus Mons, Alba Patera, and Elysium, as well as Lunae Planum. Water-ice clouds were also prominent in the Hellas and Argyre basins, possibly forming the northern edge of a wintertime south polar hood. The water-ice cloud-belt abruptly dissipated between L_s =141° and 145°. At this time dust opacity and atmospheric temperatures began to increase, thereby raising water condensation levels to much higher altitudes. Similar low-latitude belts of water-ice clouds have been observed in past Mars years during this season both in Viking data (for example, [*Tamppari et al*, 2000; *Christensen*, 1998]), from HST imaging (for example, [*Wolff et al.*, 1999; *Clancy et al.*, 1996]), and from ground-based observers (for example, [*Slipher*, 1962]). A more complete overview of observations of this aphelion season low-latitude cloud belt is given by *Pearl et al.* [2000].

The bottom panel of Plate 4 shows the distribution of water-ice clouds during the southern summer (near perihelion) season L_s =290°–310°. At this time no regional dust storms were active. To the noise level the entire southern hemisphere poleward of 20° S latitude was devoid of water-ice clouds. A few pockets of moderate cloud-opacity were still present over Tharsis, Elysium, and Lunae Planum, but there was nothing resembling the structure or intensity of the low-latitude water-ice cloud belt seen during L_s =104°–140°. To the north, poleward of about 35° N latitude, the water-ice clouds forming the polar hood are seen

near their maximum extent. Soon afterwards (see Plate 1) the edge of the north polar hood retreated northward as the season progressed to equinox. *Pearl et al.* [2000] give an overview of historical observations of the north polar hood.

5. Thermal Structure, Winds, and Waves

In this section we describe the thermal structure of the atmosphere (temperature as a function of height, latitude, longitude, and season), and the inference of wind velocities and wave structure based on the temperatures. Atmospheric temperatures are retrieved for each TES spectrum from the observed variation of radiance across the 15-μm CO_2 band by using the algorithm of *Conrath et al.* [2000]. Temperature cross-sections are formed by binning the data taken over a short period of time (typically a few days) in latitude and height (averaging all longitudes). Data from both nadir- and limb-geometry observations are used to give meaningful temperatures up to the 0.01 mbar pressure level (about 65 km). The zonal wind field may then be estimated from the temperature field by assuming gradient wind balance in the horizontal and hydrostatic balance in the vertical (for example, *Holton* [1979]). The gradient wind approximation results from assuming a balance between the horizontal pressure gradient force, the Coriolis force, and the centrifugal forces. Gradient winds cannot be computed near the equator since the assumed force balance is not valid at low latitudes. Computation of the gradient wind requires a boundary condition on the zonal wind speed which we take to be zero at the surface. Any non-zero surface wind must be added to the gradient wind result to obtain the total wind speed.

5.1. Temperature and Gradient Wind Cross-Sections

Plate 5 shows temperature and gradient wind cross-sections as observed by TES for late northern summer (L_s =135°) midway between solstice and equinox conditions. During this season thermal gradients were small in the northern hemisphere, resulting in weak winds. Near-surface atmospheric temperatures reached a maximum of about 220 K at mid-northerly latitudes. In the southern (winter) hemisphere there was a strong latitudinal gradient going into the cold polar night from the surface up to about 1 mbar. Higher in the atmosphere, temperatures first increase from equator to pole before reaching a maximum and then dropping very quickly into the cold polar night. This local temperature maximum results from adiabatic heating in the downward branch of the Hadley circulation. The location in latitude for the maximum temperature has a characteristic tilt, with the maximum occurring at higher latitudes for higher altitudes above the surface. The steep gradient in temperature between the local maximum in temperature and the cold polar night gives rise to a strong eastward jet or polar vortex reaching speeds of 100 m s^{-1} centered at 60° S latitude and 0.05 mbar. The upward branch of the Hadley circulation causes a corresponding region of cold temperatures and a westward jet over the equator. A second, much weaker, Hadley cell appears to be present in the northern hemisphere at this time. This Hadley cell causes a mild local maximum in temperature at about 60° N latitude and a corresponding weak jet of eastward winds. It forms near northern summer solstice and grows in strength as the season progresses.

Plate 6 shows temperature and gradient wind cross-sections for the northern autumnal equinox L_s =180°. With the sub-solar latitude at the equator, the thermal structure and associated wind system is now much more symmetric than at L_s =135°. Near-surface temperatures reach a maximum of about 240 K near the equator. In each hemisphere, temperatures decrease monotonically toward the pole at altitudes below about 1 mbar. Above that pressure level there is a temperature minimum at the equator and temperature maximums at mid to high latitudes in each hemisphere. The characteristic tilt of the latitude of maximum temperature with altitude above the surface is quite pronounced. Two Hadley cells are indicated (one in each hemisphere) with the northern hemisphere cell being somewhat stronger. Wind speed in the polar vortex associated with the downward branch of the northern hemisphere Hadley cell exceeds 100 m s^{-1} at 55° N latitude, while the wind speed of the southern hemisphere polar vortex reaches only about 90 m s^{-1}.

Temperature and gradient wind cross-sections for northern hemisphere winter solstice (L_s =270°) are shown in Plate 7. At solstice the maximum heating occurs at the summer pole and near-surface temperatures reach a maximum there of over 240 K. There is no indication of a southern branch of the Hadley circulation at all. In fact, throughout the southern hemisphere, atmospheric temperatures rise monotonically from equator to pole at all levels observed by

TES. This results in a hemisphere-wide zone of westward winds which reach speeds of 80 m s^{-1} or more at high altitudes above the equator. In the northern (winter) hemisphere there is a very strong latitudinal gradient in temperature between the adiabatically heated local maximum in temperature caused by the downward branch of the Hadley circulation and the very cold temperatures of the polar night. This gives rise to an intense polar jet with maximum wind speeds of 160 m s^{-1}. The strength of this Hadley circulation also causes a temperature inversion at altitudes below the 1 mbar level between 30° and 60° N latitude as cold polar air is advected toward the equator at low altitudes.

The atmospheric temperature and gradient wind results from L_s =180° and 270° described above may be directly compared with those given by *Conrath et al.* [2000] for the same seasonal period during the previous Martian year. Both sets of retrievals use TES spectra and the same retrieval algorithm and so are directly comparable. It should be noted, however, that *Conrath et al.* [2000] used only nadir-geometry data in their analysis and so they have reliable temperatures only as high as the 0.1 mbar level. The atmospheric temperature structure and wind field for L_s =180° this year (Plate 6) appears somewhat different than that for L_s =190°–200° in the previous Martian year (see Plate 2 of *Conrath et al.* [2000]). The difference in near-surface temperatures and lapse rate near the equator may be caused by a difference in the mix of local times included in the two averages with relatively more daytime temperature profiles included in this work. The difference in the strength of the southern hemisphere polar vortex is probably real, however, and is indicative of how quickly conditions change near equinox. It is quite likely that over an L_s difference of 15° (L_s =180° in this work compared with L_s =190°–200° in [*Conrath et al.*, 2000]), the southern hemisphere polar vortex wind speeds could diminish from 80 to 40 m s^{-1}. The L_s =270° results (Plate 7 in this work and Plate 3 in [*Conrath et al.*, 2000]) are at essentially the same season and are quite comparable except for near-surface temperatures at mid-southern latitudes which once again are likely different because of different proportions of daytime and nighttime spectra. Differences in the wind field at high altitudes in the southern hemisphere are probably caused by the more noisy nature of the [*Conrath et al.*, 2000] temperature cross-section.

5.2. Atmospheric Waves

Atmospheric waves play an important role in the horizontal and vertical transport of heat, momentum, and atmospheric constituents such as aerosols and water vapor. A detailed analysis of the wave modes present in the TES data is beyond the scope of this paper, but here we show an example of what the TES data potentially can provide. An earlier analysis of waves in TES aerobraking and science phasing data is given by *Banfield et al.* [2000]. Plate 8 shows maps of temperatures at the 1.36 mbar pressure level for two nearly opposite seasons. These maps show temperatures averaged over both daytime (2:00 PM local time) and nighttime (2:00 AM) data for 60 orbits (5 mapping days). What appear in the maps as temperature variations are nonmigrating wave modes that could be a mix of stationary waves and those tidal modes that interact with topography in such a way as to appear fixed in longitude. The upper panel shows 1.36-mbar temperatures for L_s =135°. There is a strong component of zonal wavenumber 2 at mid- to high-latitudes in both hemispheres. The waves have a peak-to-peak amplitude of roughly 5 K in the north and 10 K in the south. The longitude of highest temperatures are 150° and 330° W longitude in the northern hemisphere and at 120° and 300° in the southern hemisphere. Localized heating of the atmosphere over the Hellas and Argyre basins is also apparent, and the phase of the wave in the southern hemisphere appears to be related to the location of the Hellas basin. Higher in the atmosphere, at 0.3 mbar (not shown in Plate 8), the waves are not as obvious in the northern hemisphere. In the southern hemisphere, however, the zonal wavenumber 1 component becomes more pronounced with an amplitude near 10 K and maximum temperatures near 0° W longitude.

At L_s =270° the observed waves are stronger in the northern (winter) hemisphere and have very low amplitude in the southern hemisphere. In the latitude range of the polar vortex (50°–70° N latitude) the zonal wavenumber 2 component has an amplitude of about 15 K with maximum temperatures near 100° and 280° W longitude . A zonal wavenumber 1 component of amplitude 5 K and maximum temperature near 120° W longitude is also apparent. At lower northerly latitudes, from roughly the equator to 45° N latitude, a different zonal wavenumber 2 wave is prominent with peak-to-peak amplitude 10 K and maximum temperatures at 20° and 200° W longitude. At mid-southerly latitudes there is again local-

ized heating around Hellas. As at L_s =135°, at the 0.3 mbar level (not shown in Plate 8), the zonal wavenumber 1 component becomes relatively more prominent compared to the zonal wavenumber 2 component in the winter (north) mid-latitudes. The amplitude is roughly 10 K with a maximum temperature near 200° W longitude.

6. Summary

During the mapping phase of the MGS mission, the Thermal Emission Spectrometer has monitored the atmosphere of Mars for nearly a Martian year providing a view of atmospheric processes in unprecedented detail. Current routine processing gives atmospheric temperatures as a function of height in the atmosphere to 65 km and the column-integrated opacities of dust and water-ice aerosols. The retrieval of other quantities of high interest including water vapor abundance and the vertical distribution of aerosols is possible from TES data and retrieval algorithms are currently being developed.

The analysis of data returned by TES has produced significant new information about the spatial and temporal distribution of dust and water-ice clouds, and the thermal structure of the the atmosphere as a function of location and season. The complete life cycle of at least five regional dust storms has been observed. The largest regional dust storms are found to have a profound impact on the atmospheric thermal structure, raising temperatures by 15 K throughout several scale heights. Depending on the latitude and season, this direct heating of the atmosphere by dust in one hemisphere can lead to an intensification of the Hadley circulation, causing a similarly large heating almost simultaneously in the opposite hemisphere. The occurrence of water-ice clouds is sensitive to atmospheric temperatures, and the heating caused by dust storms can remove virtually all water-ice clouds from a large portion of the planet for months.

Water-ice clouds are observed to have a seasonal cycle just as distinctive as the dust seasonal cycle [*Clancy et al.*, 1996]. In the aphelion (northern summer) season when atmospheric temperature are cool, a band of low-latitude water-ice clouds was observed between 10° S and 30° N latitude where the upward motions of the Hadley circulation are expected. The cloud-belt rather abruptly vanished after L_s =140° when dust opacity and atmospheric temperatures began to increase. Soon afterwards the northern polar hood began to form and by L_s =270° had expanded as far south as 35°–40° N latitude. At all seasons (except during dust storms) water-ice clouds were observed to be common near large topographic features such as Tharsis, Olympus Mons, Alba Patera, and Elysium.

The thermal structure of the atmosphere was observed to warm and cool according to season and the distance of Mars from the Sun. Maximum atmospheric temperatures are found at the south pole at southern hemisphere solstice, while coolest temperatures are in the north polar winter night. The Hadley circulation changes from a (nearly) symmetrical two-cell configuration at equinox to a single cross-equatorial cell at solstice. At solstice the steep latitudinal temperature gradient in the winter hemisphere between a local maximum of temperature in the descending branch of the Hadley cell and the polar night causes a strong eastward jet of winds, or polar vortex, to form with speeds reaching 160 m s^{-1}. The presence of dust storms heats the atmosphere locally by as much as 15 K and can cause similar dynamical heating in the opposite hemisphere through an intensification of the Hadley circulation. Waves are common throughout the atmosphere and are especially strong in the winter mid-latitudes. Zonal wavenumber 2 dominates at lower altitudes while zonal wavenumber 1 becomes stronger at higher altitudes.

Continuing observations through the end of the nominal mapping mission of the Mars Global Surveyor will complete the monitoring of the atmosphere through one full Martian year. The possibility of an extended mission for MGS would provide an important data set for the study of the poorly understood interannual variability of Martian atmospheric phenomena.

Acknowledgments. The authors wish to thank Monte Kaelberer, Karen Horrocks, Eric Winter, and Ever Guandique for providing software development and data-handling expertise at Goddard Space Flight Center. We also thank the TES operations team at Arizona State University, including Kelly Bender, Noel Gorelick, Greg Mehall, and Kim Murray. Todd Clancy and an anonymous reviewer provided helpful comments on this manuscript. Finally, we thank the entire spacecraft and mission operations teams at the Jet Propulsion Lab and Lockheed Martin.

References

Banfield, D., B. J. Conrath, J. C. Pearl, M. D. Smith, and P. R. Christensen, Thermal tides and stationary waves on Mars as revealed by Mars Global Surveyor thermal emission spectrometer, *J. Geophys. Res., 105*, 9521–9538, 2000.

Bandfield, J. L., P. R. Christensen, and M. D. Smith, Spectral data set factor analysis and end-member recovery: Application to analysis of Martian atmospheric particulates, *J. Geophys. Res., 105*, 9573–9588, 2000.

Christensen, P. R., Variations in Martian surface composition and cloud occurrence determined from thermal infrared spectroscopy: Analysis of Viking and Mariner 9 data, *J. Geophys. Res., 103*, 1733–1746, 1998.

Christensen, P. R., et al., Thermal Emission Spectrometer Experiment: Mars Observer Mission, *J. Geophys. Res., 97*, 7719–7734, 1992.

Christensen, P. R., et al., Results from the Mars Global Surveyor Thermal Emission Spectrometer, *Science, 279*, 1692–1698, 1998.

Christensen, P. R., et al., The Mars Global Surveyor Thermal Emission Spectrometer Experiment: Investigation description and surface science results, *J. Geophys. Res.*, this issue.

Clancy, R. T., B. J. Sandor, M. J. Wolff, P. R. Christensen, M. D. Smith, J. C. Pearl, B. J. Conrath, and R. J. Wilson, An intercomparison of ground-based millimeter, MGS TES, and Viking atmospheric temperature measurements: Seasonal and interannual variability of temperatures and dust loading in the global Mars atmosphere, *J. Geophys. Res., 105*, 9553–9572, 2000.

Clancy, R. T., A. W. Grossman, M. J. Wolff, P. B. James, Y. N. Billawalla, B. J. Sandor, S. W. Lee, and D. J. Rudy, Water vapor saturation at low altitudes around Mars aphelion: A key to Mars climate?, *Icarus, 122*, 36–62, 1996.

Clancy, R. T., S. W. Lee, G. R. Gladstone, W. W. McMillan, and T. Roush, A new model for Mars atmospheric dust based upon analysis of ultraviolet through infrared observations from Mariner 9, Viking, and Phobos, *J. Geophys. Res., 100*, 5251–5263, 1995.

Conrath, B. J., J. C. Pearl, M. D. Smith, W. C. Maguire, S. Dason, M. S. Kaelberer, and P. R. Christensen, Mars Global Surveyor Thermal Emission Spectrometer (TES) observations: Atmospheric temperatures during aerobraking and science phasing, *J. Geophys. Res., 105*, 9509–9520, 2000.

Fenton, L. K., J. C. Pearl, and T. Z. Martin, Mapping Mariner 9 dust opacities, *Icarus, 130*, 115–124, 1997.

Hanel, R. A., et al., Investigation of the Martian environment by infrared spectroscopy on Mariner 9, *Icarus, 17*, 423–442, 1972.

Holton, J. R., *An Introduction to Dynamic Meteorology*, 2nd Ed. Academic Press, San Diego, 1979.

James, P. B., R. T. Clancy, S. W. Lee, L. J. Martin, R. B. Singer, E. Smith, R. A. Kahn, and R. W. Zurek, Monitoring Mars with the Hubble Space Telescope: 1990-1991 observations, *Icarus, 109*, 79–101, 1994.

Kahn, R. A., T. Z. Martin, and R. W. Zurek, The Martian dust cycle, in *Mars*, edited by H. H. Kieffer, B. M. Jakosky, C. W. Snyder, and M. S. Matthews, pp. 1017–1053. Univ. of Ariz. Press, Tucson, 1992.

Magalhães, J. A., J. T. Schofield, and A. Seiff, Results of the Mars Pathfinder atmospheric structure investigation, *J. Geophys. Res., 104*, 8943–8956, 1999.

Martin, T. Z., Thermal infrared opacity of the Martian atmosphere, *Icarus, 66*, 2–21, 1986.

Martin, T. Z., and M. I. Richardson, New dust opacity mapping from Viking infrared thermal mapper data, *J. Geophys. Res., 98*, 10,941–10,949, 1993.

Murphy, J. R., J. B. Pollack, R. M. Haberle, C. B. Leovy, O. B. Toon, and J. Schaeffer, Three-dimensional numerical simulation of Martian global dust storms, *J. Geophys. Res., 100*, 26,357–26,376, 1995.

Pearl, J. C., B. J. Conrath, M. D. Smith, J. L. Bandfield, and P. R. Christensen, Mars water-ice clouds: Observations by the Thermal Emission Spectrometer (TES) during the first martian year, *J. Geophys. Res.*, (in press), 2000.

Pollack, J. B., D. S. Colburn, R. Kahn, J. Hunter, W. Van Camp, C. E. Carlston, and M. R. Wolf, Properties of aerosols in the Martian atmosphere, as inferred from Viking lander imaging data, *J. Geophys. Res., 82*, 4479–4496, 1977.

Schofield, J. T., J. R. Barnes, D. Crisp, R. M. Haberle, S. Larsen, J. A. Magalhães, J. R. Murphy, A. Seiff, and G. Wilson, The Mars Pathfinder Atmospheric Structure Investigation/Meteorology (ASI/MET) experiment, *Science, 278*, 1752–1758, 1997.

Slipher, E. C., A photographic history of Mars 1905–1961. Northland Press. Flagstaff, Arizona, 1962.

Smith, M. D., J. C. Pearl, B. J. Conrath, and P. R. Christensen, Mars Global Surveyor Thermal Emission Spectrometer (TES) observations of dust opacity during aerobraking and science phasing, *J. Geophys. Res., 105*, 9539–9552, 2000a.

Smith, M. D., J. L. Bandfield, and P. R. Christensen, Separation of atmospheric and surface spectral features in Mars Global Surveyor Thermal Emission Spectrometer (TES) spectra, *J. Geophys. Res., 105*, 9589–9608, 2000b.

Smith, P. H., et al., Results from the Mars Pathfinder Camera, *Science, 278*, 1758–1765, 1997.

Smith, P. H., and M. Lemmon, Opacity of the Martian atmosphere measured by the Imager for Mars Pathfinder, *J. Geophys. Res., 104*, 8975–8985, 1999.

Tamppari, L. K., R. W. Zurek, and D. A. Paige, Viking era water ice clouds, *J. Geophys. Res.*, , *105*, 4087–4107, 2000.

Wolff, M. J., J. F. Bell III, P. B. James, R. T. Clancy, and S. W. Lee, Hubble Space Telescope observations of the Martian aphelion cloud belt prior to the Pathfinder

mission: Seasonal and interannual variability, *J. Geophys. Res., 104*, 9027–9041, 1999.

Zurek, R. W., J. R. Barnes, R. M. Haberle, J. B. Pollack, J. E. Tillman, and C. B. Leovy, Dynamics of the atmosphere of Mars, in *Mars*, edited by H. H. Kieffer, B. M. Jakosky, C. W. Snyder, and M. S. Matthews, pp. 835–933. Univ. of Ariz. Press, Tucson, 1992.

P. R. Christensen, Department of Geology, Arizona State University, Tempe, AZ 85287.

B. J. Conrath, Center for Radiophysics and Space Research, Cornell University, Ithaca, NY 14853.

J. C. Pearl and M. D. Smith, NASA Goddard Space Flight Center, Code 693, Greenbelt, MD 20771. (Michael.D.Smith.1@gsfc.nasa.gov)

Received July xx, 2000; revised October xx, 2000; accepted xxx xxx, 2000.

This preprint was prepared with AGU's LaTeX macros v5.01. File TES˙Mapping formatted November 2, 2000.

Plate 1. An overview of TES atmospheric observations shown as zonal averages as a function of latitude and season (L_s). The top panel shows daytime (2:00 PM local time) atmospheric temperatures at 0.5 mbar (25 km), the middle panel shows dust opacity at 1075 cm^{-1} scaled to an equivalent 6.1 mbar pressure surface, and the bottom panel shows water-ice opacity at 825 cm^{-1}. Apparent in all three panels is the effect of two large regional dust storms at L_s =225°–245°. A prominent low-latitude belt of water-ice clouds dissipated abruptly near L_s =145°.

Plate 2. Maps showing the progression of the large regional dust storms that occurred between L_s =223° and 245°. One dust storm started at L_s =223° at 0°–20° S latitude and 10°–40° W longitude. This storm spread to cover about 90° of longitude before decaying at L_s =231°. A second large regional dust storm began around L_s =227° at 0°–20° N latitude and 160°–200° W longitude. The second storm migrated to high southerly latitudes by L_s =235° before decaying near L_s =245°. The two dust storms left behind a haze throughout the southern hemisphere and low-northerly latitudes with a scaled opacity of about 0.35.

Plate 3. Maps showing the daytime (2:00 PM local time) spatial distribution of dust during three regional storms observed by TES. The top panel shows scaled dust opacity during the period L_s =170°–190°. The middle panel shows scaled dust opacity during the period L_s =260°–273°. The bottom panel shows scaled dust opacity during the period L_s =321°–350°.

Plate 4. Maps showing the daytime (2:00 PM local time) spatial distribution of water-ice cloud opacity during the northern summer (top panel; L_s =104°–140°) when the equatorial cloud belt was prominent, and during the souther summer (bottom panel; L_s =290°–310°) when the north polar hood of clouds was prominent.

Plate 5. Mean meridional cross-sections of retrieved atmospheric temperatures (top panel) and gradient wind speeds (bottom panel) for L_s=135° (late northern summer). Temperatures are in kelvins and wind speeds are in m s^{-1}. Positive wind speeds are eastward. The mean surface pressures for this data set are indicated at the lower boundary of the contoured regimes.

Plate 6. Mean meridional cross-sections of retrieved atmospheric temperatures (top panel) and gradient wind speeds (bottom panel) for L_s=180° (northern hemisphere fall equinox). Temperatures are in kelvins and wind speeds are in m s^{-1}. Positive wind speeds are eastward. The mean surface pressures for this data set are indicated at the lower boundary of the contoured regimes.

Plate 7. Mean meridional cross-sections of retrieved atmospheric temperatures (top panel) and gradient wind speeds (bottom panel) for L_s=270° (northern winter solstice). Temperatures are in kelvins and wind speeds are in m s^{-1}. Positive wind speeds are eastward. The mean surface pressures for this data set are indicated at the lower boundary of the contoured regimes.

Plate 8. Maps showing the horizontal variation of atmospheric temperatures at 1.36 mbar during 5-sol periods centered at L_s =135° (top panel) and L_s =270° (bottom panel). Planetary-scale waves are apparent as the systematic variation of temperature as a function of longitude around a latitude circle.

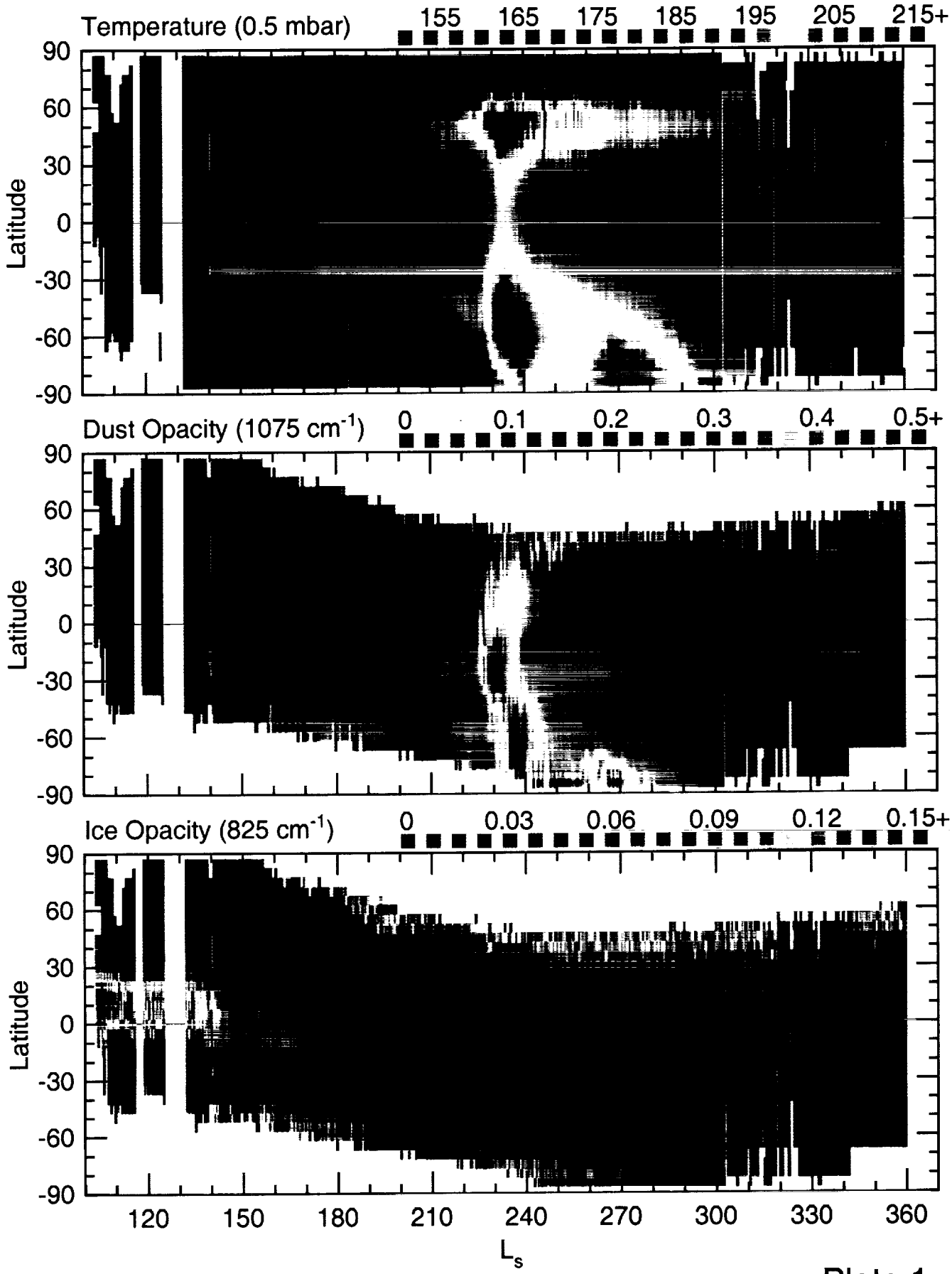
Temperature (0.5 mbar)
155 165 175 185 195 205 215+
Dust Opacity (1075 cm-1)
0 0.1 0.2 0.3 0.4 0.5+
Ice Opacity (825 cm-1)
0 0.03 0.06 0.09 0.12 0.15+
Latitude
90 60 30 0 -30 -60 -90
120 150 180 210 240 270 300 330 360
Ls

Plate 1

Thermal Emission Spectrometer (TES) Observations of Dust Opacity

9-micron dust opacity:

0.1 0.2 0.3 0.4 0.5 0.75

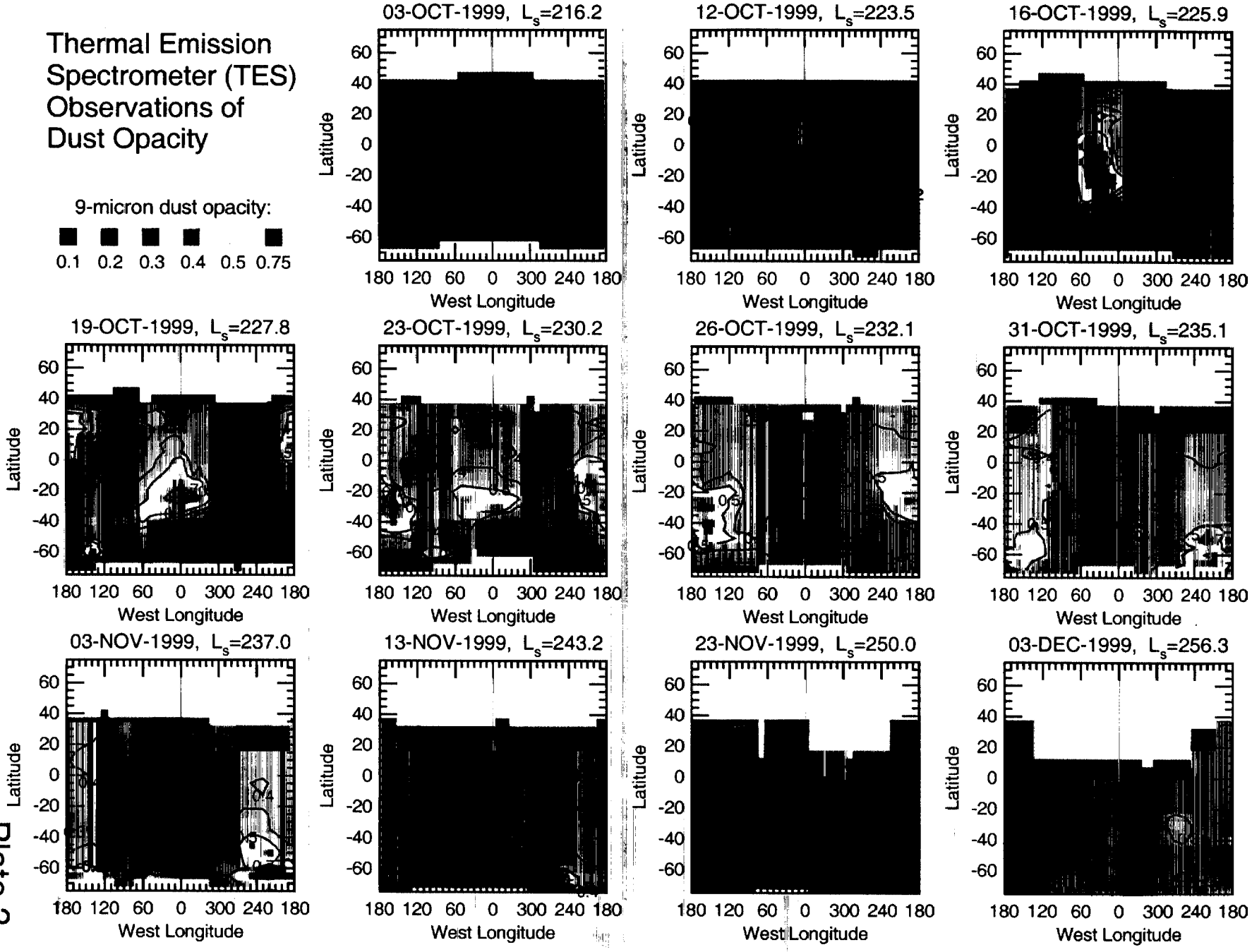

Plate 2

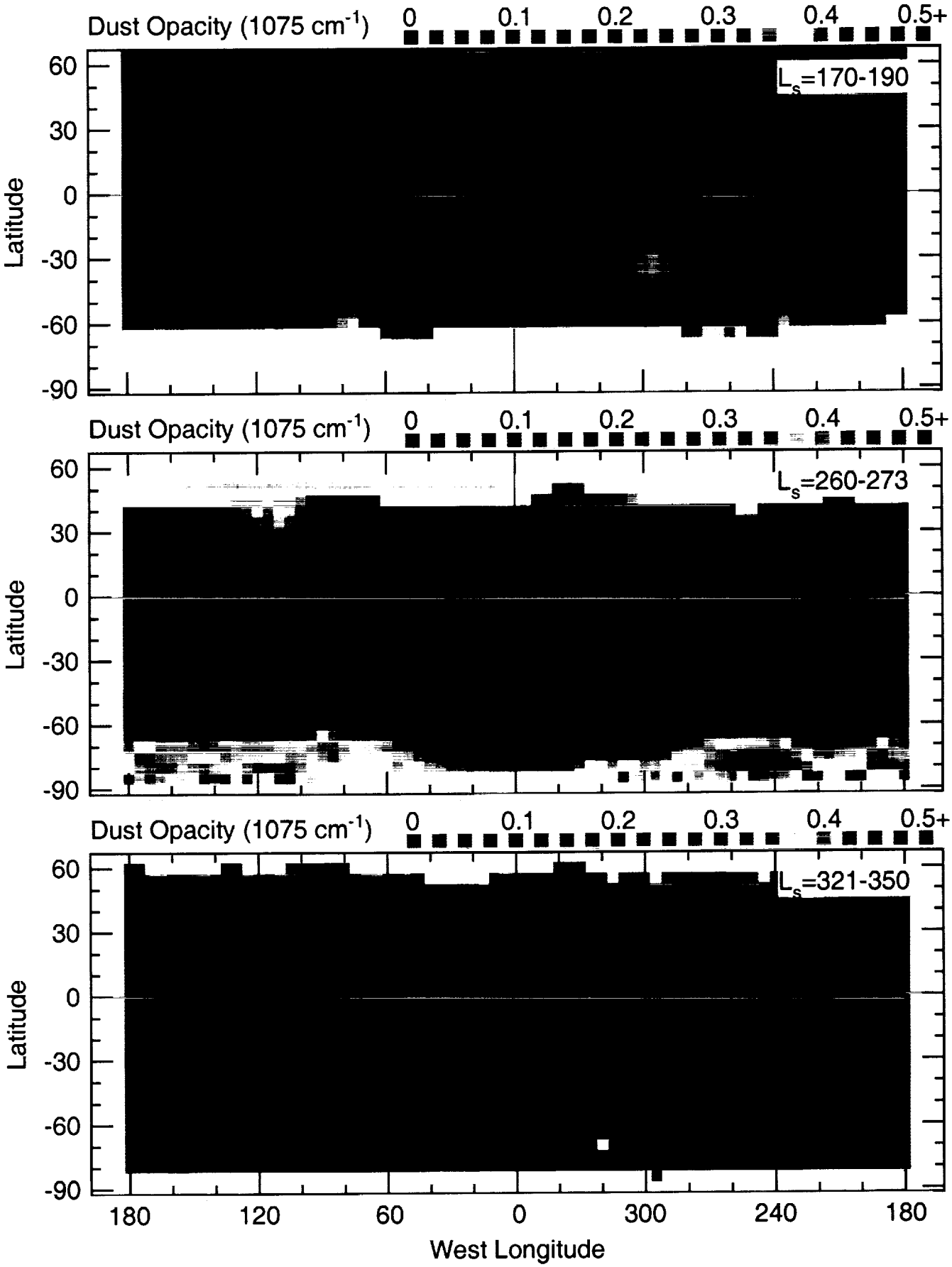
Dust Opacity (1075 cm-1)
0
0.1
0.2
0.3
0.4
0.5+
Ls=170-190
Ls=260-273
Ls=321-350
Latitude
60
30
0
-30
-60
-90
180
120
60
0
300
240
180
West Longitude

Plate 3

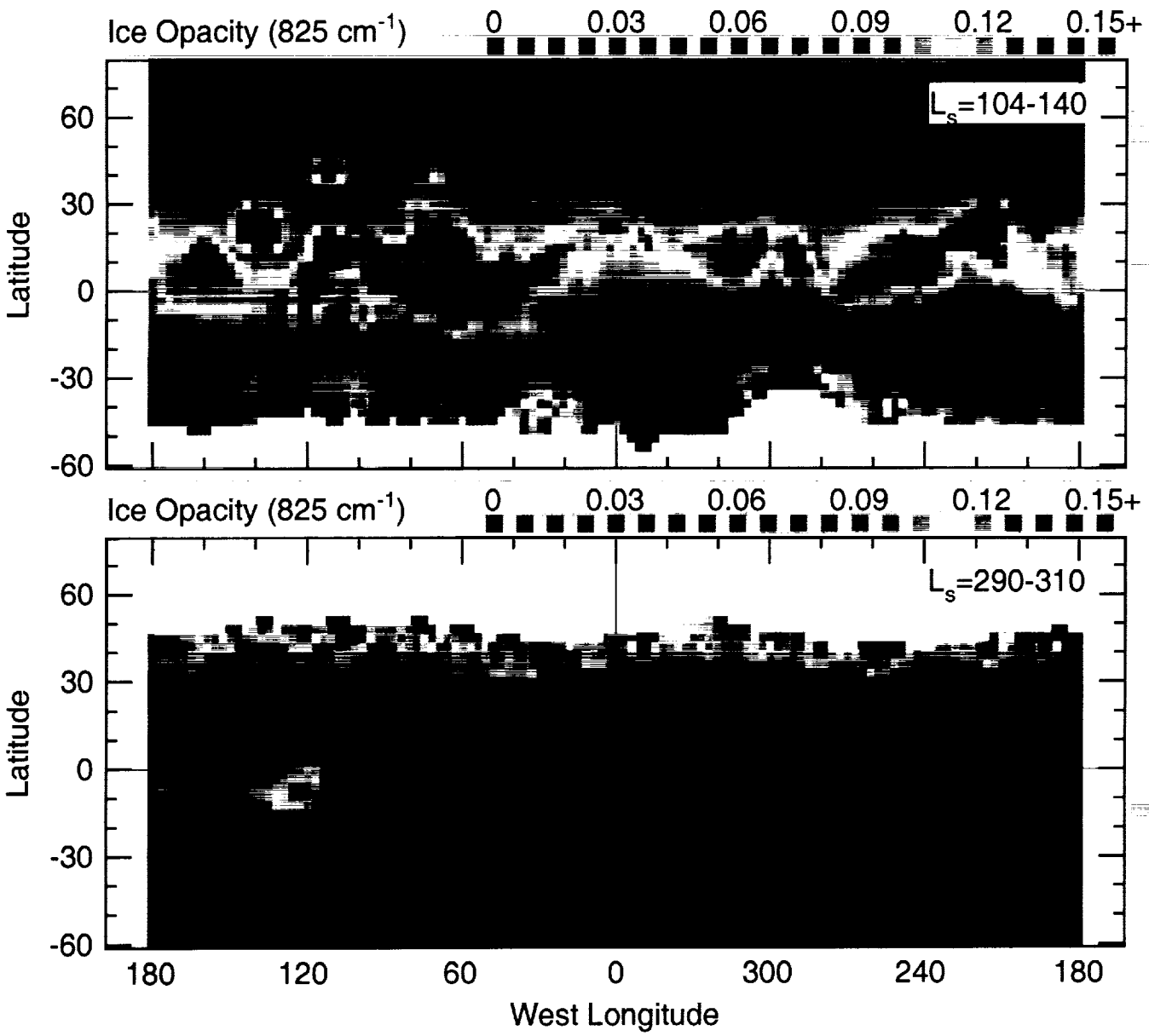
Ice Opacity (825 cm^{-1})
0
0.03
0.06
0.09
0.12
0.15+
L_s=104-140
60
30
0
-30
-60
Latitude
Ice Opacity (825 cm^{-1})
0
0.03
0.06
0.09
0.12
0.15+
L_s=290-310
60
30
0
-30
-60
Latitude
180
120
60
0
300
240
180
West Longitude

Plate 4

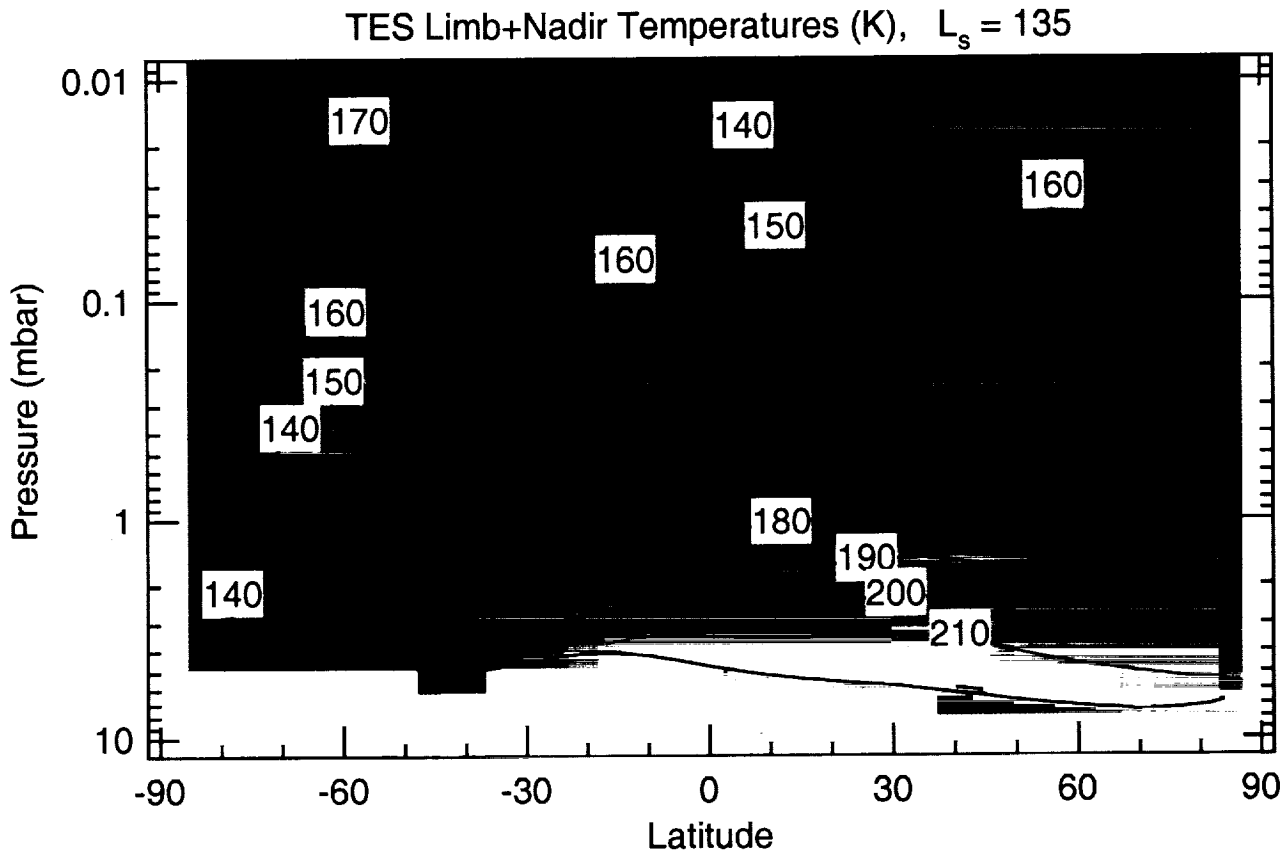
TES Limb+Nadir Temperatures (K), L_s = 135
Pressure (mbar)
0.01
0.1
1
10
170
140
160
150
160
160
150
140
180
190
200
210
140
-90
-60
-30
0
30
60
90
Latitude

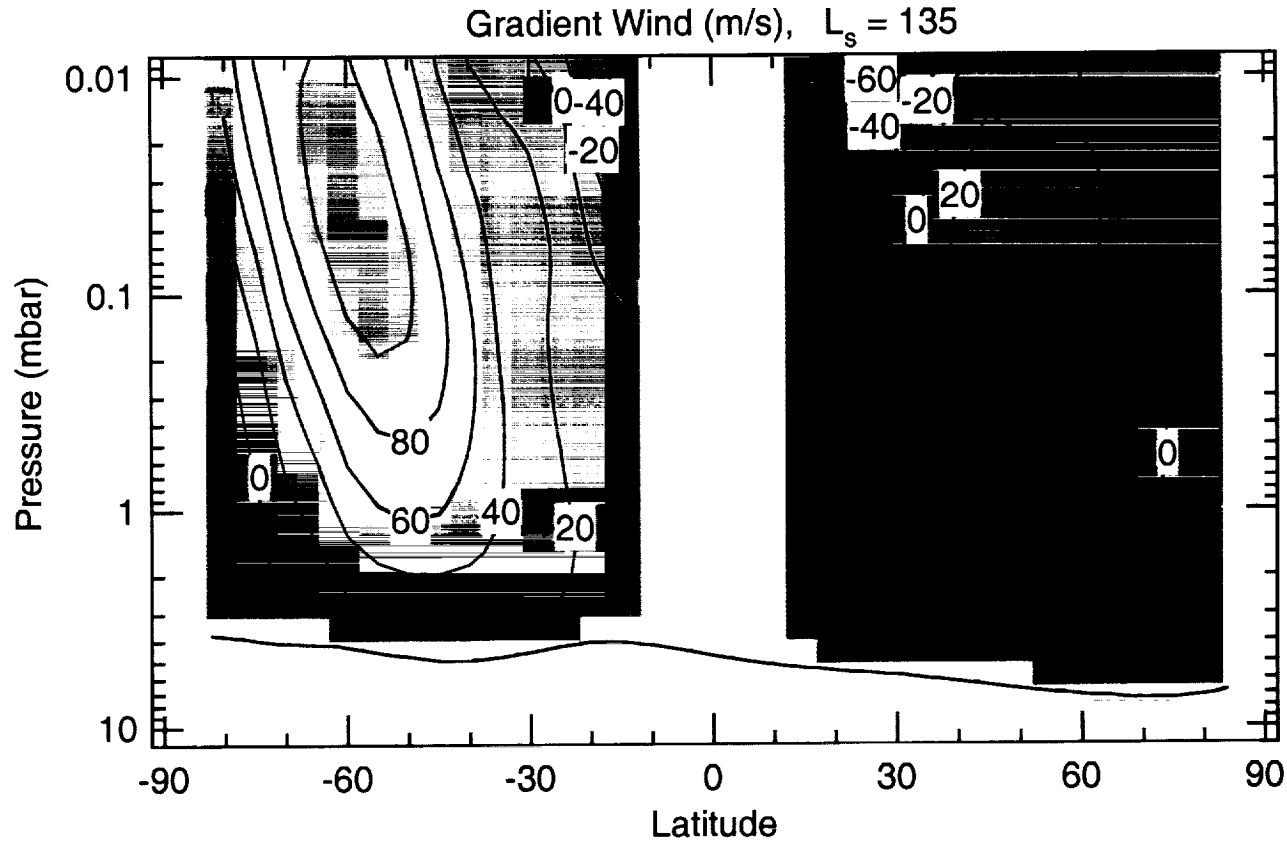
Gradient Wind (m/s), L_s = 135
Pressure (mbar)
0.01
0.1
1
10
0-40
-20
-60
-20
-40
20
0
80
0
60
40
20
0
-90
-60
-30
0
30
60
90
Latitude

Plate 5

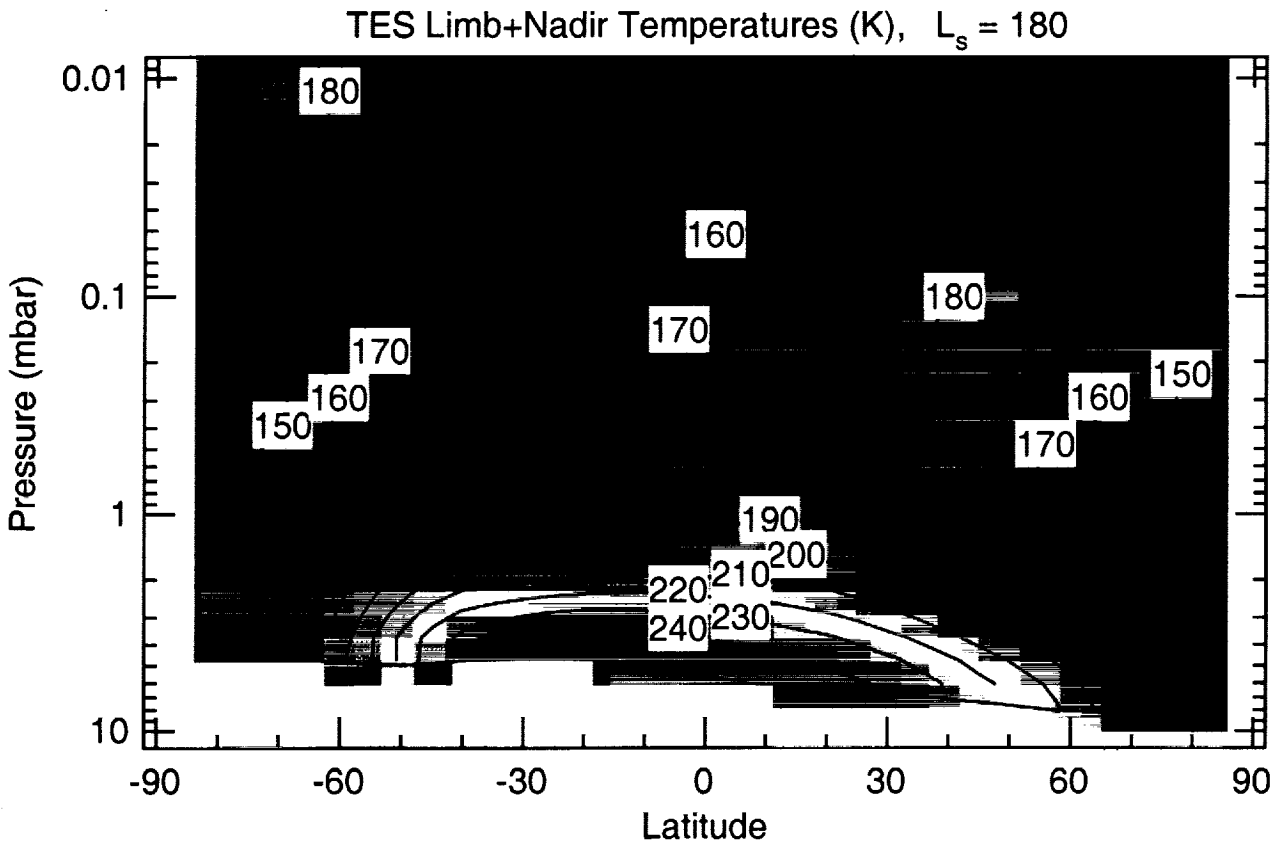
TES Limb+Nadir Temperatures (K), L_s = 180
Pressure (mbar)
0.01
0.1
1
10
180
160
170
150
190
200
210
220
230
240
-90
-60
-30
0
30
60
90
Latitude

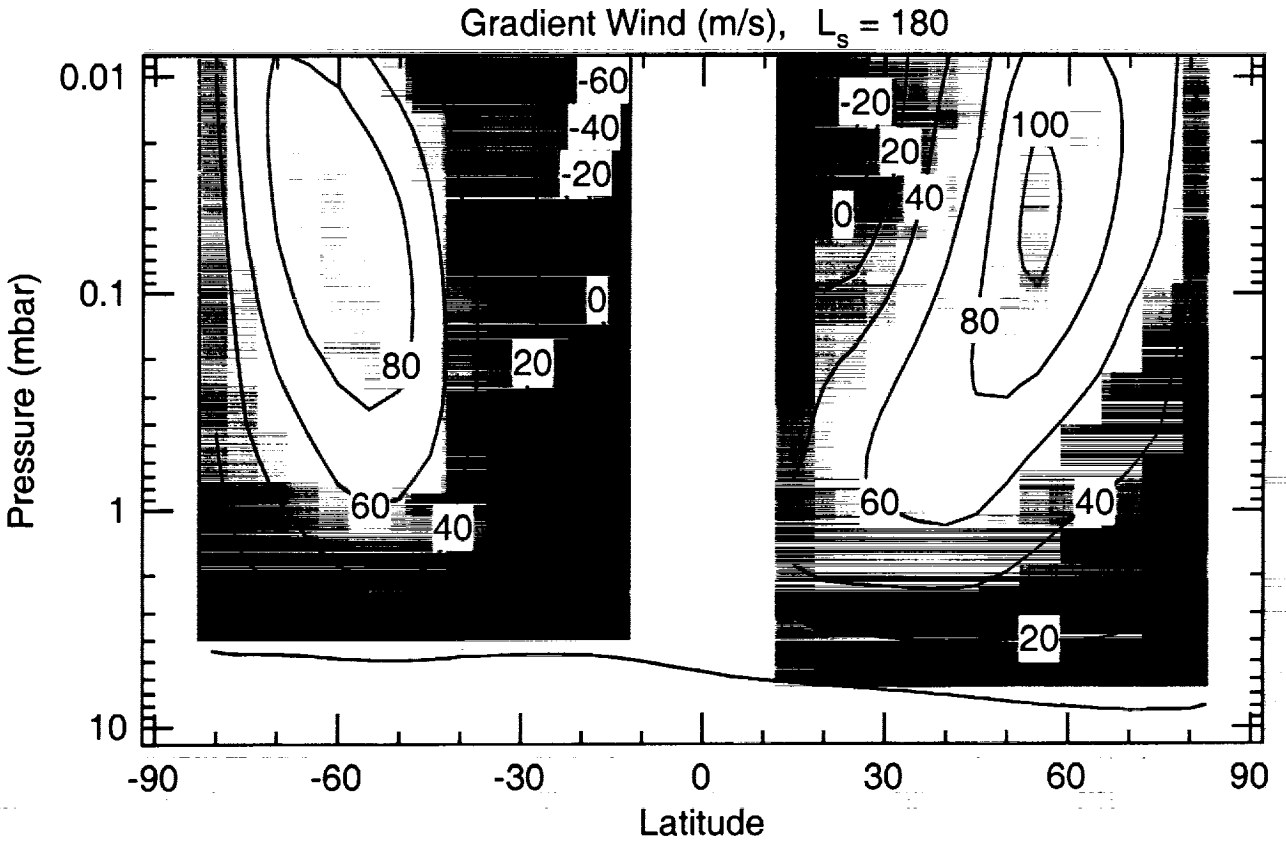
Gradient Wind (m/s), L_s = 180
Pressure (mbar)
0.01
0.1
1
10
-60
-40
-20
0
20
40
60
80
100
-90
-60
-30
0
30
60
90
Latitude

Plate 6

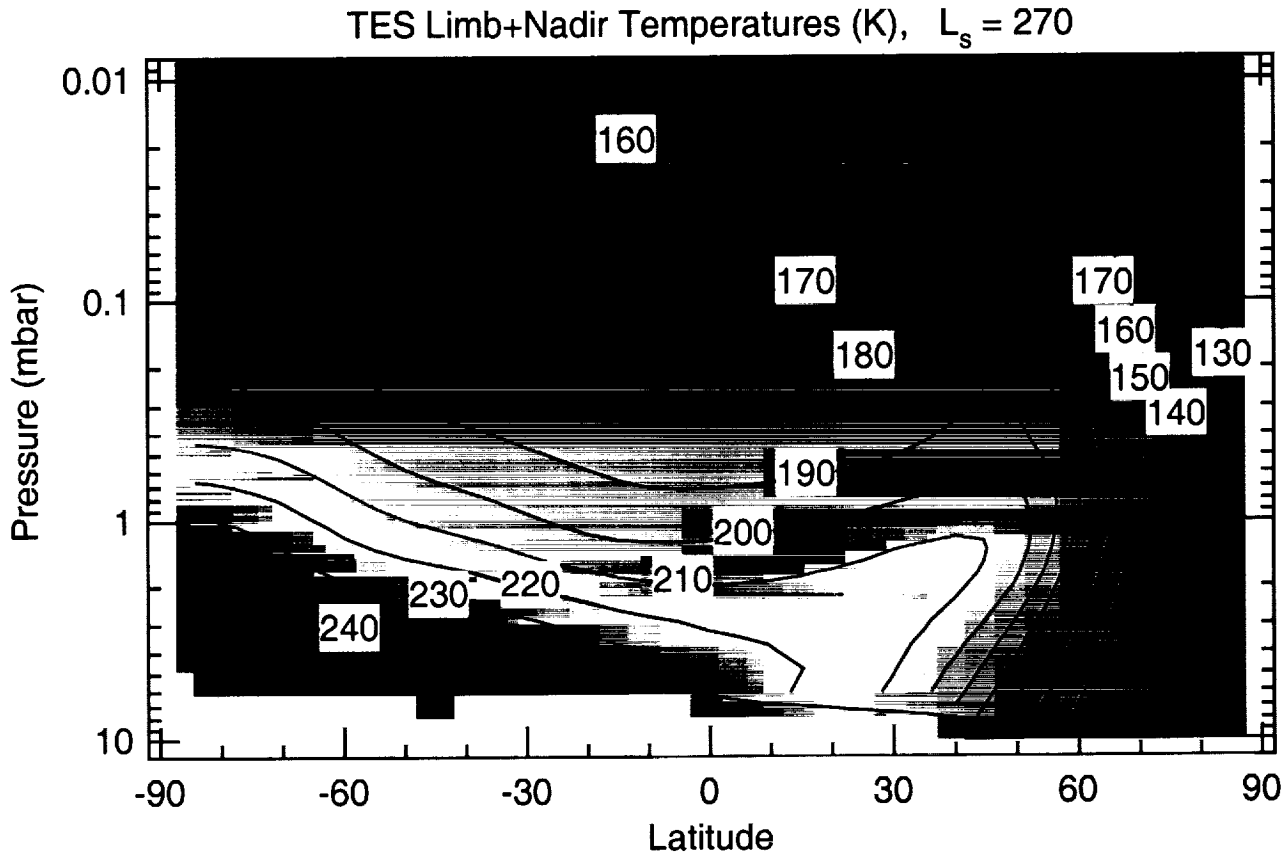
TES Limb+Nadir Temperatures (K), L_s = 270
Pressure (mbar)
0.01
0.1
1
10
160
170
180
190
200
210
220
230
240
170
160
150
140
130
-90
-60
-30
0
30
60
90
Latitude

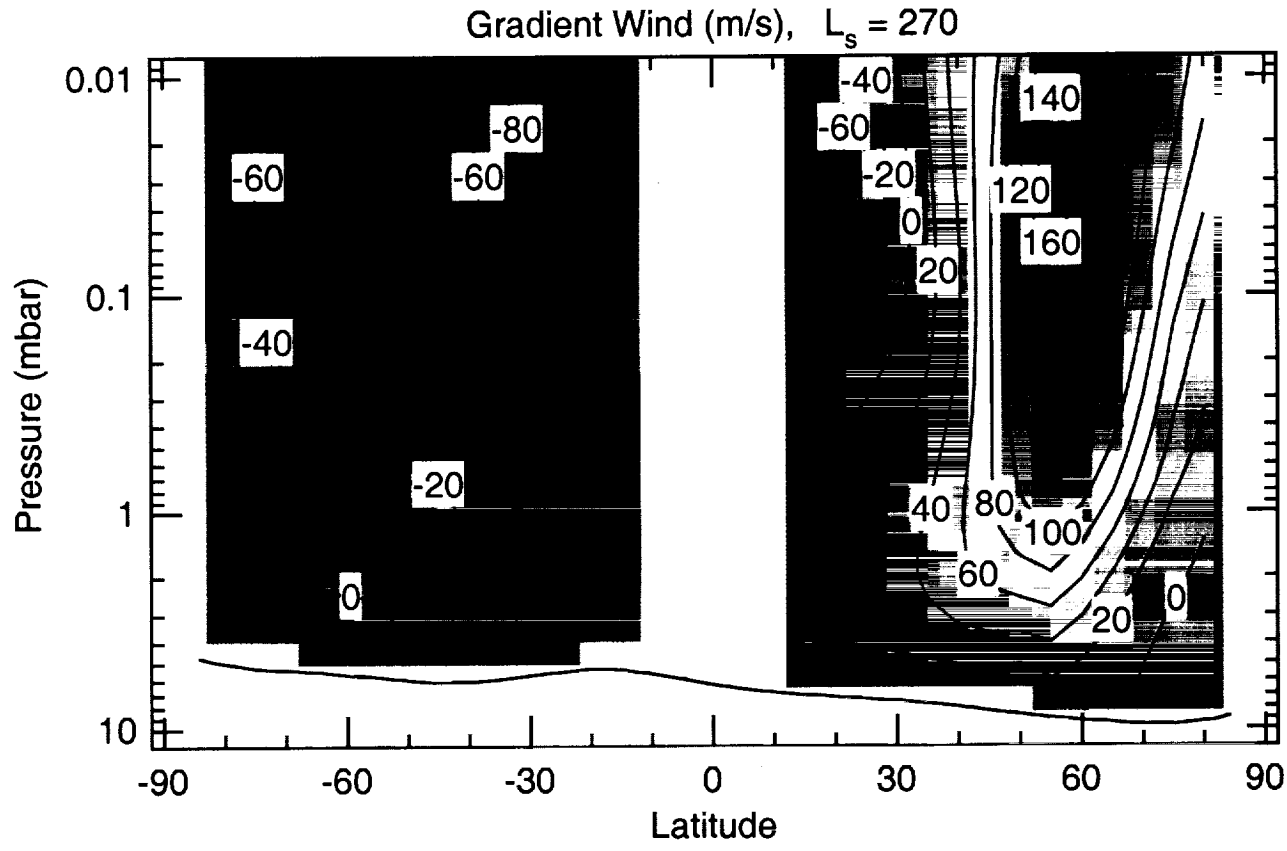
Gradient Wind (m/s), L_s = 270
Pressure (mbar)
0.01
0.1
1
10
-80
-60
-60
-40
-20
0
-40
-60
-20
0
20
140
120
160
40
80
100
60
20
0
-90
-60
-30
0
30
60
90
Latitude

Plate 7

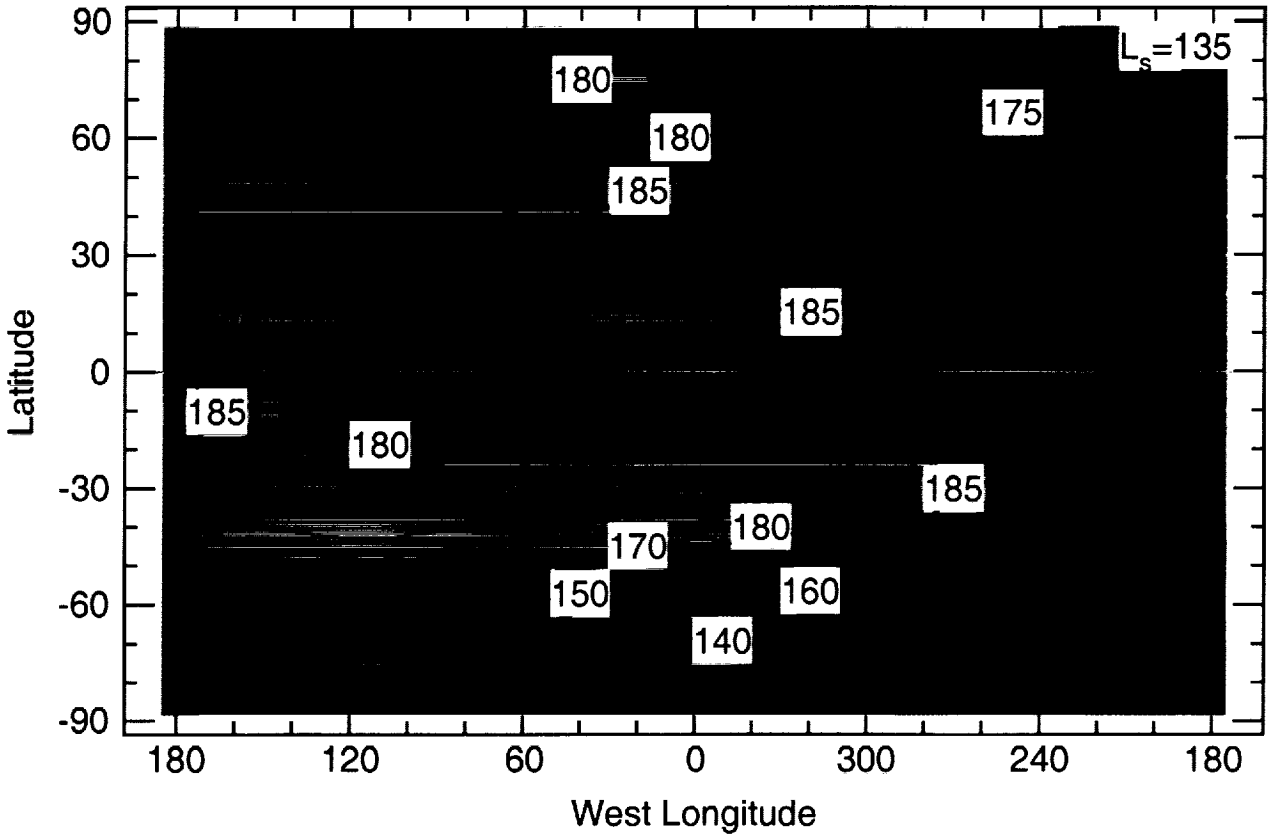
L_s=135
180
180
185
175
185
185
185
180
185
170
180
150
160
140
90
60
30
0
-30
-60
-90
180
120
60
0
300
240
180
Latitude
West Longitude

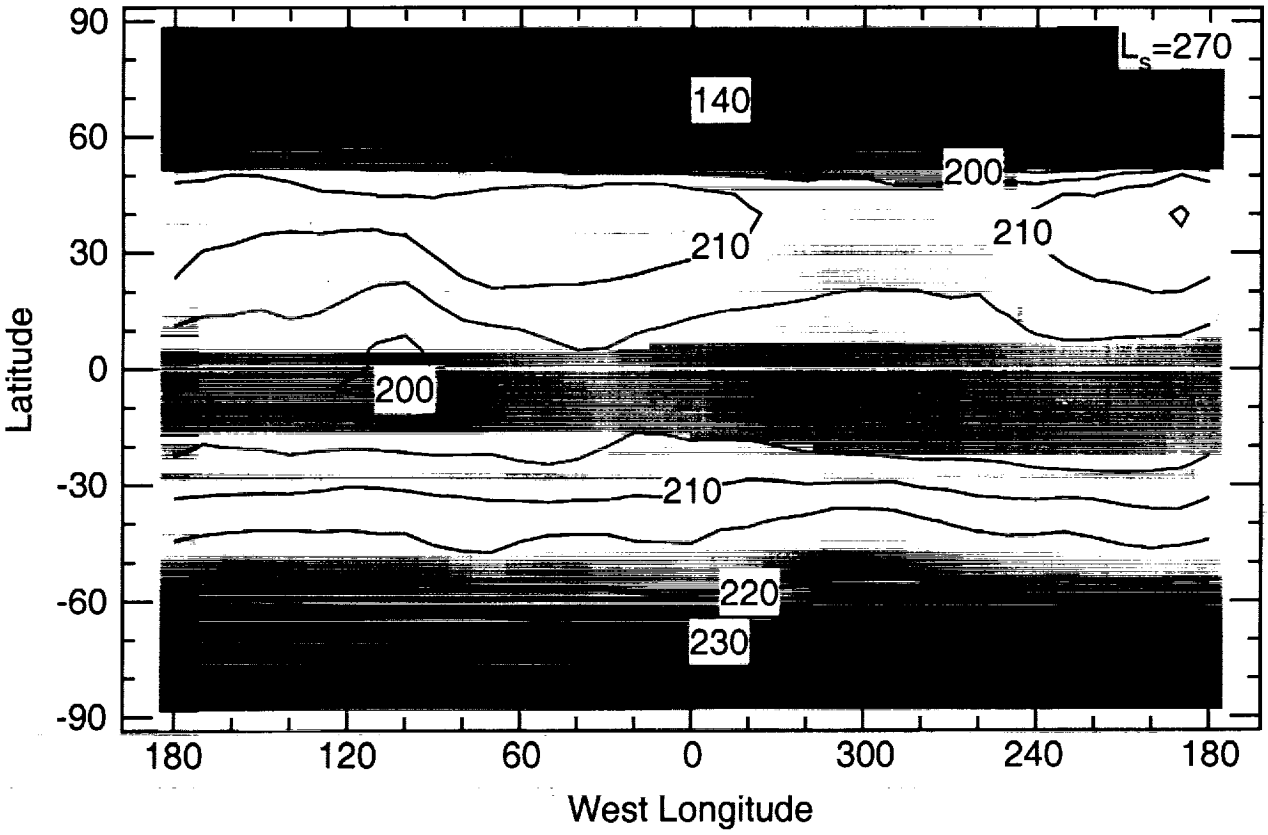
L_s=270
140
200
210
210
200
210
220
230
90
60
30
0
-30
-60
-90
180
120
60
0
300
240
180
Latitude
West Longitude

Plate 8